



Engineering the oxygen vacancies enables Ni single-atom catalyst for stable and efficient C-H activation

Jinwei Wu^a, Jie Gao^{a,b,*}, Shuangshuang Lian^a, Jianpeng Li^a, Kaihang Sun^c, Shufang Zhao^d, Young Dok Kim^d, Yujing Ren^b, Meng Zhang^a, Qiaoyun Liu^a, Zhongyi Liu^{a,**}, Zhikun Peng^{a,**}

^a Green Catalysis Center, College of Chemistry, Henan Institute of Advance Technology, Research Institute of Industrial Technology, Zhengzhou University, Zhengzhou 450001, PR China

^b Interdisciplinary Research Center of Biology & Catalysis, School of Life Sciences, Northwestern Polytechnical University, Xi'an 710072, PR China

^c School of Chemical Engineering and Technology, Tianjin University, Tianjin 300072, PR China

^d Department of Chemistry, Sungkyunkwan University, Suwon 16419, Republic of Korea



ARTICLE INFO

Keywords:

Single-atom catalysts
Oxygen vacancy
C-H activation
Carbon deposition

ABSTRACT

Ni single-atom catalysts (SACs) can perform with the extremely high activity in the activation of the C-H bond, however, deactivation caused by carbon deposition became the main obstacle for commercialization. Herein, Ni/CeO₂ SAC was synthesized and employed in dry reforming of methane (DRM) reaction. The oxygen vacancies (O_V) with different concentrations were successfully regulated on CeO₂ surface by the replacement of Ce⁴⁺ cation by a smaller-size cation M (M= Mg, Co, Zn). The catalyst with the highest O_V concentration has performed with the highest activity retention and a high turnover frequency of methane (14.5 s⁻¹). During the DRM process, along with the increase of the O_V concentration from 21.9% to 30.8%, the amount of carbon deposition decreased by 50%. The effective C-H activation function from Ni SACs and CO₂ activation function from O_V were synergistically combined, leading to a high activity of methane conversion and an effective carbon removal process in the O_V-SAC catalytic system. This work provides a novel strategy to obtain a robust O_V-SAC catalytic system for efficient and stable C-H activation.

1. Introduction

The C-H activation is a crucial step for hydrocarbons utilization [1, 2]. Ni-based catalysts with low price and high activity are widely used in C-H activation [3–5]. However, the severe deactivation induced by the sintering of Ni nanoparticles as well as the carbon deposition at high temperatures restricts its industrial applications [6,7]. Recently, Ni single-atom catalyst (SAC) has attracted more and more attention due to the high atomic utilization and exact uniform active sites [8,9]. Compared to Ni nanoparticles, the atomically dispersed Ni atoms have shown stronger metal-support interaction, which can effectively suppress the aggregation of Ni atoms at high temperatures [10–13]. While the carbon deposition caused by the dissociation of hydrocarbons over isolated Ni active sites during the C-H activation reaction is the main obstacle for stable and efficient C-H activation [14]. Designing and developing a strategy to remove the deposited carbon at high activity is

an effective way to improve the stability of Ni SAC.

The *in-situ* adsorbed oxygen (O_{ad}) species adjacent to the Ni single atoms are highly effective reactants to eliminate carbon deposition, and the O_{ad} species are usually generated on the oxygen vacancies (O_V) [15]. Hence, the carbon deposition can be probably solved by constructing sufficient O_V around the Ni single atoms. As an O_V-containing support, CeO₂ was widely used in catalysis and the O_V are defects of CeO₂ in essence [16,17]. In previous studies, the single metal atoms are usually anchored at O_V over the CeO₂ support by forming the M-Ce bond [18, 19], which can greatly decrease the O_V concentration and result in the decline of stability. Generally, CeO₂ with limited O_V was an optional support for carbon removal but the rate of carbon deposition is always much higher than that of coke elimination. Therefore, increasing the O_V concentration on the Ni/CeO₂ SAC is a promising way to improve the catalytic stability in C-H activation. The formation of O_V over CeO₂ support can be attributed to the existence of Ce³⁺ and other cations

* Corresponding author at: Green Catalysis Center, College of Chemistry, Henan Institute of Advance Technology, Research Institute of Industrial Technology, Zhengzhou University, Zhengzhou 450001, PR China.

** Corresponding authors.

E-mail addresses: jgao@nwpu.edu.cn (J. Gao), liuzhongyi@zju.edu.cn (Z. Liu), ZhikunPeng@163.com (Z. Peng).

smaller than Ce⁴⁺ on CeO₂[20], hence the O_V concentration can be regulated by introducing smaller-size cations and increasing Ce³⁺ concentration [21].

In this work, a robust O_V-SAC catalytic system (Ni/M-CeO₂ SACs) were synthesized by a facile precipitation-hydrothermal method. The O_V concentration was successfully regulated by doping series of smaller-size cation M (M=Mg, Co, and Zn) over CeO₂ surfaces. Compared to the Ni/CeO₂ NPs, the Ni/CeO₂ SACs presented high initial activity in dry reforming of methane (DRM) reaction. Ni/M-CeO₂ SACs with more O_V continued to show higher activity within the 150-h reaction. The amount of carbon deposition decreased by 50% along with the increase of the O_V concentration from 21.9% to 30.8%. This synergistic effect between isolated Ni atoms and O_V achieved continuous high activity. This work proposed a promising O_V-SAC model catalyst to obtain an efficient and stable catalyst for C-H activation.

2. Experiment

2.1. Catalyst preparation

Ni/CeO₂ SACs were prepared by the modified precipitation-hydrothermal method[22]. Firstly, 16.8 g of NaOH and 0.004 mol metal nitrate precursors were dissolved in 70 mL and 10 mL deionized water, respectively. Then, nitrate solution was added into NaOH solution dropwise under vigorous stirring at ambient temperature. The obtained suspension liquid was transferred into a 100 mL hydrothermal reactor and maintained at 120 °C for 1500 min. After cooling down naturally, the slurry was washed with deionized water and dried at 110 °C overnight. Finally, the powder was calcined at 400 °C for 2 h to obtain the employed catalysts. The prepared Ni/CeO₂ SAC and Ni SAC with a second metal M were named as Ni₁/Ce and Ni₁/Mce (Ni₁/MgCe, Ni₁/CoCe, and Ni₁/ZnCe), respectively. The theoretical loading weight of Ni and M were 2.5 wt% and 1.25 wt%. In addition to the Ni-based catalysts, the M/CeO₂ catalysts (Mg/CeO₂, Co/CeO₂, and Zn/CeO₂) were also prepared by the above method. Pure CeO₂ was also prepared by the same method without the addition of Ni or M. Additionally, a Ni/CeO₂ nanoparticles (Ni/Ce NPs) catalyst with the theoretical loading weight of 2.5 wt% was obtained by the equivalent-volume impregnation method. The measured water absorption quantity of CeO₂ is 700 $\mu\text{L g}^{-1}$. Then, Ni (NO₃)₂•6 H₂O solution was loaded on CeO₂. After drying it at 110 °C for 12 h, the samples were obtained by calcining at 400 °C for 2 h.

2.2. Catalyst characterization

Transmission electron microscope (TEM) images were performed with a JEOL JEM-2011 instrument operated at an accelerating voltage of 200 kV. Aberration-corrected HAADF-STEM (AC-HAADF-STEM) and corresponding high-resolution elemental mapping of energy dispersive X-ray (EDX-mapping) spectroscopy images were obtained by Titan ETTEM Themis and Super X EDS equipped on the microscope.

The X-ray absorption spectra (XAS) including X-ray absorption near-edge structure (XANES) and extended X-ray absorption fine structure (EXAFS) of the sample at XX-edge was collected at the Beamline of TPS44A1 in National Synchrotron Radiation Research Center (NSRRC), Taiwan, China. X-ray diffraction (XRD) patterns were recorded using a PANalytical X'Pert PRO instrument with Cu-K α radiation ($\lambda = 1.5418 \text{ \AA}$). And the data was collected with a scan range from 5° to 90° at a scan speed of 0.03°.

X-ray Photoelectron Spectroscopy (XPS) results of samples was obtained on a ThermoFischer ESCALAB 250Xi X-ray photoelectron spectrometer. The valence electrons were excited using a monochromatized Al K α source ($h\nu = 1486.6 \text{ eV}$) and the pass energy was 50 eV with energy step of 0.05 eV. All binding energies were calibrated by using that of C 1 s (284.8 eV). Raman experiments were conducted on a confocal Raman Spectroscopy (LabRAM HR Evolution, HORIBA Jobin Yvon), and the wavelength was set as 325 nm and 532 nm for fresh

samples and spent samples, respectively. The electron paramagnetic resonance (EPR) tests were carried out on the X-band (9.84 GHz) with 4.00 G modulation amplitude and a magnetic field modulation of 100 kHz using a EPR spectrometer (EMXPlus-10/12, Bruker) at 77 K. The samples were tested without any pretreatment in the XPS, Raman, and EPR experiments.

The *in-situ* XPS measurements were carried out in a customized SPECS UHV system equipped with a SPECS PHOIBOS 150 analyzer, a SPECS XR50 X-ray source, and a SPECS 1D DLD detector. The base pressure of the system is better than $3 \times 10^{-10} \text{ mbar}$. The samples were pre-reduced with 10% H₂/Ar (50 mL min⁻¹) at 600 °C for 2 h and then pressed onto stainless steel mesh for further XPS measurements. The samples were first put into the modified load lock chamber and reduced in 10 mbar H₂ at 200 °C for 1 h, then transferred to the XPS chamber for characteristic after cooling to about 300 K.

All chemisorption experiments were carried out on a Micromeritics AutoChem 2950 HP, which is connected to an online mass spectrometer. In H₂-TPR experiment, 100 mg of samples were purged in Ar flow (50 mL min⁻¹) at 400 °C for 60 min to remove the impurities and adsorbed water. After cooled down to 50 °C under flowing Ar, the sample was heated to 600 °C at a rate of 10 °C min⁻¹ under a gas mixture of 10% H₂ in Ar as the reductant. The effluent gas was recorded by a thermal conductivity detector (TCD). As for temperature-programmed desorption (CO₂-TPD and O₂-TPD), the 100 mg of sample was reduced with 10% H₂/Ar (50 mL min⁻¹) at 600 °C for 60 min. After cool down to 50 °C under flowing Ar, the gas of adsorbate (CO₂ or O₂, 50 mL min⁻¹) was introduced at the same temperature for 60 min. Subsequently, He flow (50 mL min⁻¹) was admitted to purged the physically adsorbed species for 60 min. It was then heated to 700 °C at a rate of 10 °C min⁻¹ under flowing helium (50 mL min⁻¹). The effluent gas was recorded by a TCD. In O₂-TPO reaction, 30 mg of the sample was exposed under the 10% O₂-Ar flow (50 mL min⁻¹) from 50 °C to 800 °C (10 °C min⁻¹). The CO (*m/e* = 28) and CO₂ (*m/e* = 44) signals were analyzed by the online mass spectrometer (HIDEN Analytical Decra Gas analysis system).

The temperature-programmed surface reaction (TPSR) was performed on the same instrument with chemisorption. 100 mg of the sample (0.1 g) was firstly pre-reduced in 10% H₂/Ar (50 mL min⁻¹) flow at 600 °C for 60 min and then cooled down to 50 °C under He atmosphere (50 mL min⁻¹). The reactant gas (CH₄ or CO₂, 50 mL min⁻¹) was admitted into catalysts with the temperature increasing to 800 °C (10 °C min⁻¹). The signals were recorded by the equipped online mass spectrometer. Notably, an H₂-TPR experiment was carried out after CO₂-TPSR.

In-situ pulse experiments were conducted by the same instrument with TPSR above. 50 mg of the sample was reduced by 10% H₂/Ar (50 mL min⁻¹) flow at 600 °C for 60 min. Then, the sample was heated to 800 °C (10 °C min⁻¹) at He atmosphere (30 mL min⁻¹). Pulses with the loop volume of 0.5 mL were auto injected into the catalyst bed by the following sequence: 9 pulses of CH₄; 3 pulses of CO₂; 1 pulse of CH₄. The signals of effluent gas were recorded by the equipped online mass spectrometer (HIDEN Analytical Decra Gas analysis system). The amount of O_{ad} species during pulse experiments was calculated by the sum of the amount of CO and twice the amount of CO₂ (the details were shown in Eq. S7 in the supporting information). The coke amount was calculated by the difference between CH₄ consumption and the CO evolution and CO₂ evolution (details are shown in Table S7 in the supporting information).

2.3. Catalytic testing

The activity and stability tests were carried out on a fixed-bed reactor. Firstly, 400 mg quartz sand and 100 mg catalyst were well mixed and transferred into the reactor. Before reaction, 30 mL min⁻¹ 10% H₂/Ar was used to pretreated catalyst at 600 °C for 1 h. After prerduction, the mixed gas of CO₂, CH₄, and Ar (CO₂/CH₄/Ar=1/1/3, gas hourly space velocity (GHSV) of 30000 mL g⁻¹ h⁻¹) was

introduced into the reactor at the target temperature. The effluent gas was analyzed by an online gas chromatograph (Agilent GC 7820). The ratio of H₂/CO and the conversions of CH₄ and CO₂ were calculated by Eq. S4 and Eq. S3 in the supporting information, respectively.

3. Results and discussion

3.1. Atomically dispersed Ni

The morphology properties of catalysts were obtained by the TEM images. As shown in Fig. 1a, the Ni₁/CoCe catalyst displayed the same nanorod structure as the Ni₁/Ce catalyst (Fig. S1), indicating the doping of Co did not change the morphology of CeO₂. In AC-HAADF-STEM images (Fig. 1b), the lattice spacing of 0.32 nm and 0.28 nm can be assigned to the (111) and (200) planes of CeO₂, respectively. It is difficult to directly distinguish Ni and Co atoms on CeO₂ due to the lower contrast of Ni and Co atoms compared to Ce atom [22]. The

AC-HAADF-STEM and the corresponding high-resolution EDS characterization were conducted to investigate the dispersion of Ni and Co species. On the one hand, the 512 × 512 mapping resolution with a sampling pixel size as small as ~0.05 nm was used to probe the localized elemental distribution in the 25 nm × 25 nm ROI for EDS mapping (Figs. 1e and S2). In this case for a ~1 nm nanoparticle of Ni or Co species supported on the CeO₂ surface, there would be aggregated 400 probing pixels (20 × 20) in EDS images. Obviously, in all observed regions there are exclusively no aggregation of Ni or Co elements according to EDS mapping images (Figs. 1e and S2). On the other hand, as shown in Table S1 and Fig. 1f, the Ni and Co atomic fraction confirmed the existence of both Ni and Co species. Based on the above analysis, it demonstrated the atomic dispersion of Ni and Co on CeO₂ surface.

Consequently, a few darker atoms in pink circles among the light Ce atoms matrix can be considered as Ni single atoms (Fig. 1b). In addition, the configuration modified by DFT calculations suggests the doping of Co atoms on CeO₂ could induce position deviation and O_V (Fig. 1d).

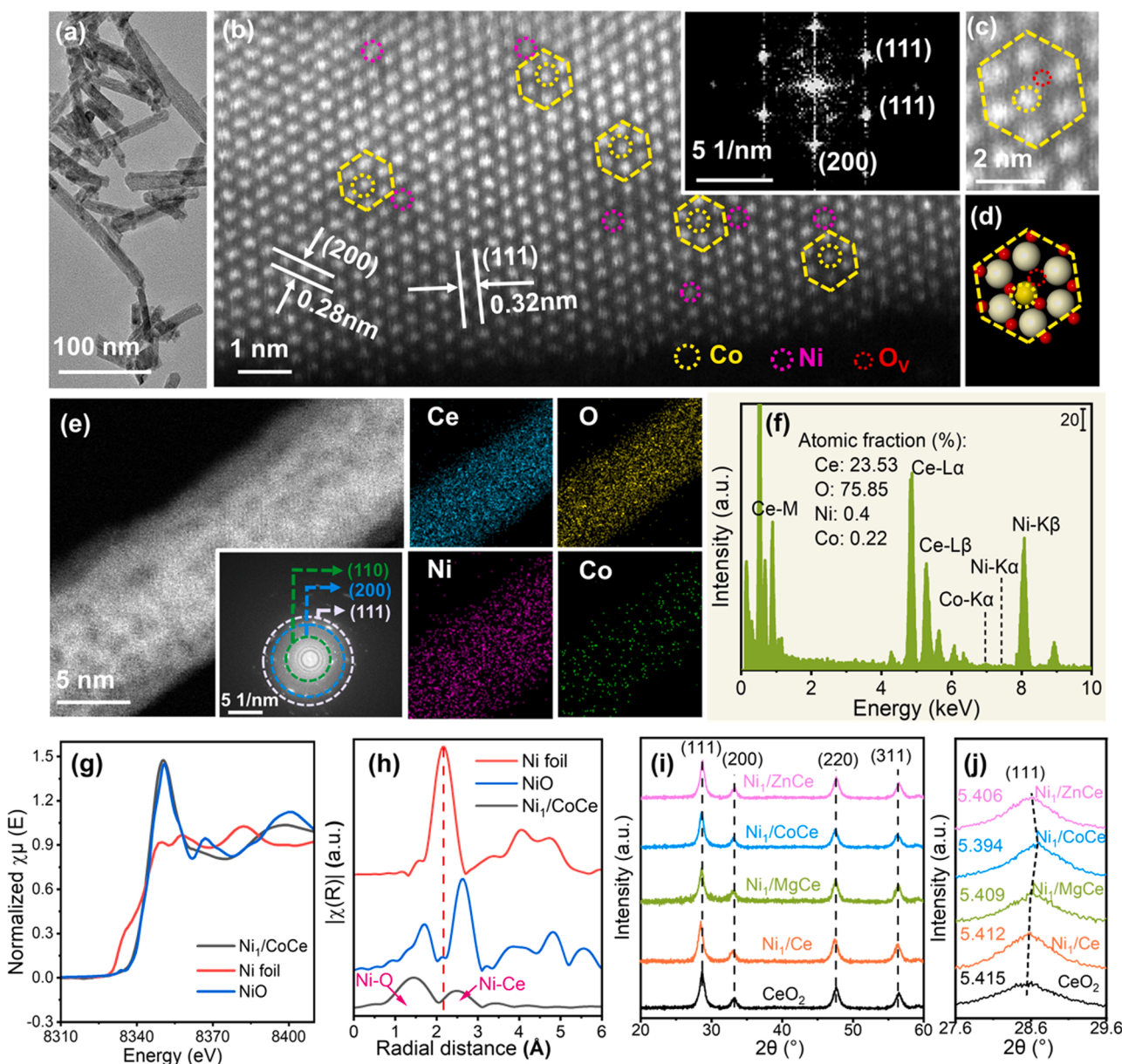


Fig. 1. (a) TEM, (b) AC-HAADF-STEM with an inset FFT images, (c) atomic-resolution images of typical Ni₁/CoCe and (d) the corresponding configuration optimized by DFT calculations. (e) EDX mapping and (f) the corresponding EDS analysis of Ni₁/CoCe. (g) Ni K-edge XANES and (h) R-space spectra of Ni₁/CoCe and referenced samples. XRD patterns with (i) the region of 2θ at 20–60° and (j) the region of 2θ at 27.6–29.6° of the fresh samples, the inset values are lattice parameters of CeO₂.

Therefore, the smaller-size and position-deviated atoms are most probably Co atoms (Fig. 1c). Combining with the following analysis of O_V species, it can be speculated that O_V are located in the red circles on CeO₂ (Fig. 1c). Based on above results and analysis, a novel O_V-SAC synergistic catalytic model catalyst involving isolated Ni atoms and O_V was successfully constructed.

X-ray absorption spectroscopy (XAS) was conducted to determine the coordination environment of Ni atoms. The feature of Ni₁/CoCe X-ray absorption near-edge structure (XANES) closely resembles NiO standard samples, manifesting that the valence of Ni in Ni₁/CoCe is close to that in NiO (Fig. 1g). According to the R-spectra data of Ni foil and NiO standard samples, the lengths of the Ni-O bond and Ni-Ni bond are 1.7 Å and 2.2 Å, respectively (Fig. 1h). The absence of the Ni-Ni bond confirmed that the Ni atoms were atomically dispersed in Ni₁/CoCe. It is consistent with aberration-corrected TEM results. In addition, Ni₁/CoCe exhibited strong Ni-O scattering and an obvious 2.60 Å contribution attributed to the Ni-Ce scattering [8], indicating that Ni was primarily coordinated with O atoms and a few Ni atoms were combined with Ce atoms.

To figure out the impact of Co atoms, the CO-DRIFT was conducted on the reduced samples (Fig. S4a). The large peak at 1960 cm⁻¹ of the Ni/Ce NPs catalyst can be attributed to the bridge adsorption between Ni⁰ and CO molecule, confirming that the Ni atoms exist in form of Ni nanoparticles. No peak was observed on the Ni₁/Ce and Ni₁/CoCe catalysts, suggesting that the absence of the Ni nanoparticles. In addition, the Ni₁/CoCe exhibited similar profiles with Ni₁/Ce, indicating the impact of M on Ni was negligible and O_V are the major considered factor in DRM reaction.

The series of prepared catalysts with different O_V concentrations exhibited the similar actual Ni loading weight from ICP results (Table S2). No diffraction peaks of NiO or M oxide were detected due to the absence of NiO clusters or nanoparticles (Fig. S4). As shown in Fig. 1i, all catalysts have similar four diffraction peaks at 28.5°, 33.1°, 47.6°, and 56.4°, respectively corresponding to the (111), (200), (220) and (311) planes of CeO₂. Notably, peaks at 28.5° of the Ni₁/CoCe catalyst shifted a bit compared with the Ni₁/Ce catalyst (Fig. 1j), indicating that Co atoms were doped onto the CeO₂ matrix, coinciding with

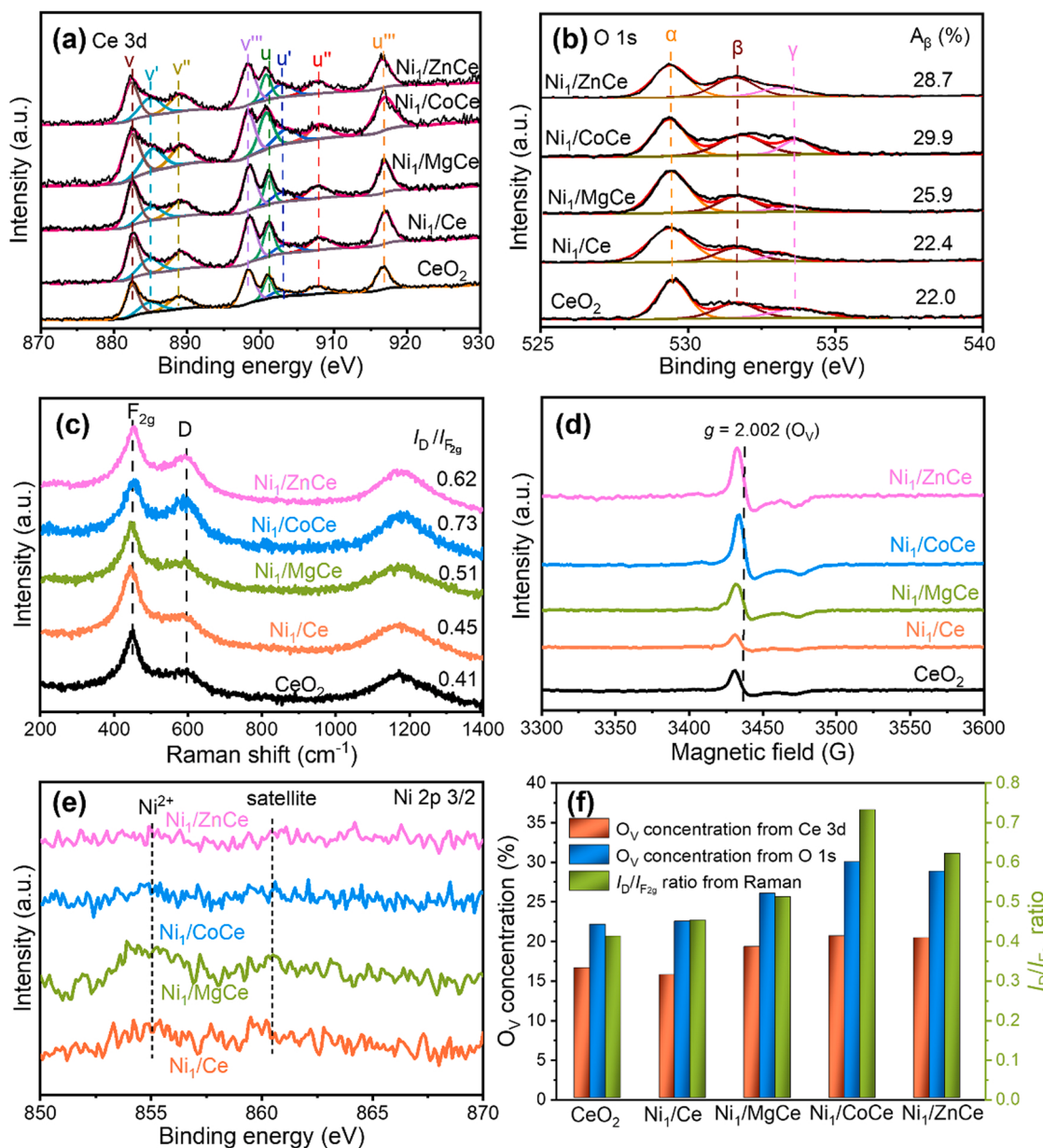


Fig. 2. Characterizations of oxygen vacancy. (a-e) Ce 3d spectra, O 1 s spectra, Raman spectra, EPR spectra, and Ni 2p spectra of the fresh samples. (f) The calculated O_V concentration results of the fresh samples.

the aberration-corrected TEM results. Besides, the lattice parameters of CeO_2 were calculated and shown in Table S2. The lattice parameters of Ni_1/MCe are lower than that of CeO_2 , indicating that the second metal M were doped onto the CeO_2 lattice and resulted in lattice contraction. Wherein, the doping of Co atoms leads to the largest lattice contraction. In addition to O_V , the doping of the second metal could induce other types of defects on CeO_2 [23]. These other defects may have influences on the catalytic process, such as thermal stability, phase segregation, etc. [24]. Considering the employed Ni_1/MCe catalysts have the similar thermal stability and other structure properties, this work mainly focused on the effect of O_V on carbon removal. The specific surface area and pore information of catalysts were obtained by the N_2 -physisorption experiments (Fig. S4b). Compared with the pure CeO_2 , Ni_1/Ce remained the high specific surface area after calcination, suggesting better thermal stability was achieved. Besides, Ni_1/MCe exhibited similar N_2 physisorption isotherms profiles, indicating that the introduction of M did not change the pore structure and distribution.

3.2. Oxygen vacancies

To analyze the surface O_V over the catalysts, XPS experiments were conducted. In Ce 3d spectrum (Fig. 2a), u and v peaks represent the spin-orbit splitting of Ce $3d_{5/2}$ and Ce $3d_{3/2}$, respectively. Among them, the peaks labeled u'' , u''' , u' , u'' , v'' , v' , and v are attributed to the Ce^{4+} species and the peaks named as u' and v' are ascribed to the Ce^{3+} species [25, 26]. The O_V on CeO_2 surface are formed by the surface Ce^{3+} species, thereby the O_V concentration can be calculated by the Ce^{3+} proportion (Eq. S1) [27]. The calculated results of the employed catalysts are shown in Fig. 2a. Compared with the CeO_2 , Ce^{3+} proportion on Ni_1/MCe was obviously increased. Notably, Ce^{3+} proportion was increased from 15.6% to 20.5% by doping the Ni_1/Ce catalyst with Co atoms (Table S3). In the O 1 s spectra (Fig. 2b), the peaks centered at 529 eV (α), 530.5 eV (β), 532.5 eV (γ) are assigned to the lattice oxygen, oxygen species in

surface O_V , and chemisorbed oxygen species, respectively [28–30]. Wherein, β peaks are generally regarded as O_V [31,32]. Thus, O_V concentration can be estimated by the fraction of β peaks according to Eq. S2. The calculated results in Table S3 reveal that the Ni_1/CoCe exhibits the highest O_V concentration. In addition, Fig. S5 shows the concentration of O_V increased with increasing Co content to a level and then decreased with further increment of Co content. This decrease is attributed to the aggregation of Co atoms [29].

In the Raman spectra (Fig. 2c), all employed catalysts show two bands at 450 cm^{-1} (F_{2g}) and 596 cm^{-1} (D), corresponding to the symmetrical stretching F_{2g} mode of Ce-O and O_V , respectively [33,34]. No NiO signal at 520 cm^{-1} is observed due to the atomically dispersion of Ni. It is reported that the O_V concentration of CeO_2 can be quantified by the peak intensity ratio of D/ F_{2g} [35]. The O_V concentration calculated by Raman results follow the same order as XPS results (Fig. 2f). The lower intensity of F_{2g} bands on Ni_1/MCe catalysts are attributed to the structure distortion induced by the smaller-size M cation doping into the CeO_2 lattice matrix. Additionally, the F_{2g} bands of Ni_1/MCe shifted towards a larger wavenumber compared to Ni_1/Ce due to the longer average length of Ce-O bonds derived from the substitution of Ce^{4+} cation with the smaller-size M cation. In EPR spectra (Fig. 2d), all samples exhibited obvious peaks ($g=2.002$), which can be used for the identity of O_V on CeO_2 [36,37]. The intensity of peaks on all samples follow the same sequence with XPS and Raman results.

The *in-situ* XPS results were employed to investigate and confirm the O_V concentration in the quasi-reaction condition (Fig. 3a-b). The calculated O_V concentration of the reduced catalysts follow the same sequence with that of the fresh catalysts. By doping Co atoms, the O_V concentration was increased from 21.9% to 30.8%. Notably, the Ce^{3+} proportion of the reduced catalysts were raised due to the reduction of partial Ce^{4+} . However, the area proportion of the β peaks were not obviously changed due to the pretreatment in reducing atmosphere and the vacuum test system. Besides, the *in-situ* reduced catalysts and fresh

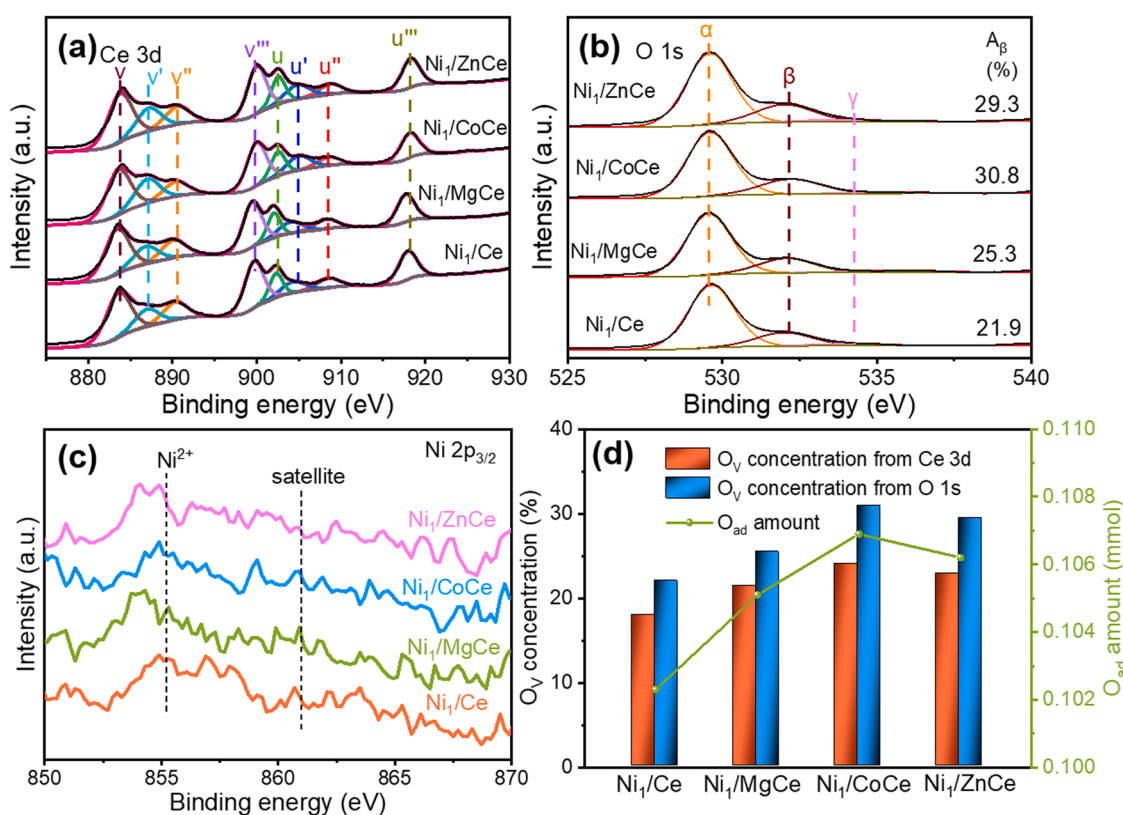


Fig. 3. (a) Ce 3d, (b) O 1 s, and (c) Ni 2p photoemission features from *in-situ* XPS studies of the reduced samples (d) Calculated O_V concentration results from *in-situ* XPS studies of the reduced samples (bar profiles) and calculated O_{ad} amount of the reduced samples during the following *in-situ* pulse experiments (line profiles).

catalysts both exhibited weak signals in the Ni 2p spectra due to the high dispersion of Ni atoms on CeO₂ surface (Figs. 2e and 3c). Moreover, the *in-situ* pulse experiments were conducted on the reduced samples to quantify O_{ad} species on O_V at the simulated actual reaction condition (analysis details will be discussed in the following mechanism section). The amount of O_{ad} species was calculated by the sum of the amount of CO and twice the amount of CO₂ (the details were shown in Eq. (S7) in the supporting information). The calculated amount of O_{ad} species shown in Fig. 3d are consistent well with the *in-situ* XPS results. Combined with the above results, it demonstrates that O_V was successfully created on CeO₂ surface by doping second metal cations and can be maintained in the reducing atmosphere.

H₂-TPR experiments were carried out for all catalysts to investigate the redox properties of catalyst surface (Fig. 4a). It is always considered that higher metal dispersion leads to a higher reduction temperature [38]. The reduction temperature of Ni₁/Ce is much higher than that of Ni/Ce NPs, according well with the high dispersion isolated Ni atoms on Ni₁/Ce. The profiles of H₂ consumption on the Ni₁/Ce and Ni₁/MCE catalyst can be divided into three peaks: α (250 °C), β (350 °C) and γ (400 °C), corresponding to the reduction of O_{ad} on O_V, highly dispersed Ni²⁺ and Ce⁴⁺ respectively [25]. The H₂ consumption occurs at a similar temperature on Ni₁/Ce and Ni₁/MCE catalysts. This indicates that the coordination environment of isolated Ni atom is basically the same, and the M cations have no obvious contribution for the strong metal support interaction (SMSI). As for the Ni/Ce NPs catalyst, the α' peak should be attributed to the reduction of NiO NPs dispersed on CeO₂ surface [39]. The surface basicity strength of employed catalysts were determined by CO₂-TPD (Fig. 4b). The desorption peaks of all samples can be distinguished into three regions: 50–200 °C (α), 200–400 °C (β), and 400–600 °C (γ), corresponding to weak, medium, and strong basic sites [29,40]. Obviously, the Ni₁/MCE expose more weak and medium alkaline sites on the surface of CeO₂ than Ni/Ce NPs. O₂-TPD was used to detect the chemisorption effect of O_V on oxygen species. All samples displayed three similar desorption peaks at the range of 50–300 °C (α), 300–600 °C (β), and 600–700 °C (γ) respectively (Fig. 4c). Wherein, the β peaks are regarded as the O_{ad} species on vacancies [41,42]. The desorption amounts of oxygen species follow the sequence: Ni₁/CoCe > Ni₁/ZnCe > Ni₁/MgCe > Ni₁/Ce, which is consistent with O_V concentration based on XPS and Raman results.

3.3. Synergistic effects between O_V and Ni single atoms for the C-H activation

The effect of O_V on enhancing atomically dispersed Ni stability was investigated in the DRM process. As a typical methane conversion reaction, DRM can convert CH₄ and CO₂ into syngas with the theoretical CO/H₂ molar ratio of 1.0, which is suitable for Fischer-Tropsch synthesis [43–45]. The higher reaction temperature always leads to higher activity due to the endothermic nature of DRM reaction [46,47]. As shown in Fig. S7, the catalysts performed high activity at 800 °C and the CH₄ conversion is close to the equilibrium conversion. Therefore, the

stability tests of the catalysts were carried out at 800 °C. As shown in Fig. 5c, the H₂/CO ratio of employed catalysts are below 1.0 because of the presence of reverse water-gas shift (RWGS) reaction (CO₂ + H₂ → CO + H₂O). Besides, M/CeO₂ catalysts (Mg/CeO₂, Co/CeO₂, and Zn/CeO₂) exhibited negligible activity in the same reaction condition compared with the Ni₁/Ce catalyst (Fig. 5a-c). Ni/Ce NPs has a high initial activity, but a dramatic decline of activity was observed due to carbon deposition and the aggregation of Ni NPs (Fig. 5a-c). Compared to Ni/Ce NPs, Ni₁/Ce catalyst performed with a higher initial conversion and turnover frequency (TOF) of methane at 800 °C (Fig. 5a and Table S5) due to the extremely high intrinsic activity of atomically dispersed Ni atoms. However, the Ni₁/Ce catalyst loses activity as a result of the carbon deposition caused by CH₄ decomposition (CH₄ → C + 2 H₂) with time on stream (verified by the following O₂-TPO results and TG results). On the other hand, catalysts with the presence of O_V allow the formation of O_{ad} (originated from CO₂ adsorption and activation), which readily removes the deposited carbon thereby sustaining the high activity for over 150 h. Thus, catalysts with higher O_V concentration show the higher activity retention after a 150 h DRM reaction (Fig. 5d). Wherein, Ni₁/CoCe with the highest O_V concentration (30.8%) performed the highest activity retention (96.5%) after 150 h DRM reaction and exhibited both extremely high stability and activity compared with other reported counterpart catalysts (Table S6). Besides, O_V concentration of the employed catalysts maintained the initial order after 150 h DRM reaction (Fig. S8), suggesting that the O_V on CeO₂ were stable during methane conversion. Consequently, it demonstrates that our O_V-SAC catalytic system provides a highly efficient and stable C-H activation.

The activation of the C-H bond on Ni active sites is the rate-determining step in the DRM process [48,49]. To investigate the activation of methane on isolated Ni atoms, the *in-situ* CH₄-TPSR experiments were carried out. All catalysts exhibited CH₄ consumption and H₂ evolution peaks due to the deep dissociation of CH₄ on Ni atoms (CH₄ → C + 2 H₂). Wherein, the CH₄ dissociation on Ni₁/Ce occurred at a lower temperature than that on Ni/Ce NPs (Fig. 6a), suggesting the higher activity on isolated Ni atoms (in agreement with catalyst evaluation results). During the CH₄-TPSR process, carbon deposition was accumulated and resulted in rapid deactivation of the catalysts. All the samples exhibited no CH₄ consumption at about 800 °C, indicating the Ni sites were capsulated by the carbon deposition. The Ni₁/CoCe catalyst with the highest O_V concentration consumed the most CH₄ and produced the most H₂ at the same time (Fig. 6b). This demonstrates that the O_{ad} species on O_V can effectively remove the carbon deposition on isolated Ni atoms, and the coke removal effect will become obvious with the increase of O_V concentration.

As shown in Fig. 6c, all the catalysts exhibited two peaks in CO signals. Wherein, limited by the instruments, the peaks at higher temperatures were incomplete. According to the following *in-situ* sequential pulse experiments (Fig. 8c), the Ni₁/CoCe catalyst exhibited the most CO production. Based on the results of sequential pulse experiments, it is speculated that CO evolution on the Ni₁/CoCe is the most of all the

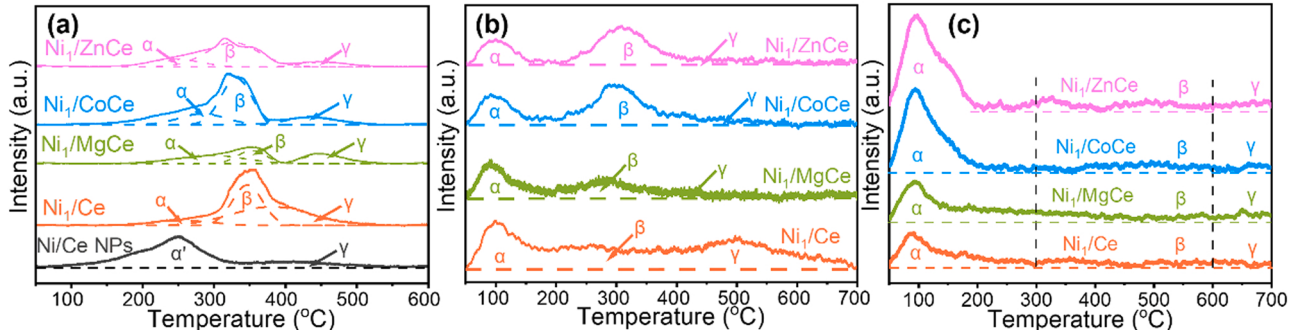


Fig. 4. (a) H₂-TPR, (b) CO₂-TPD, and (c) O₂-TPD profiles of the samples.

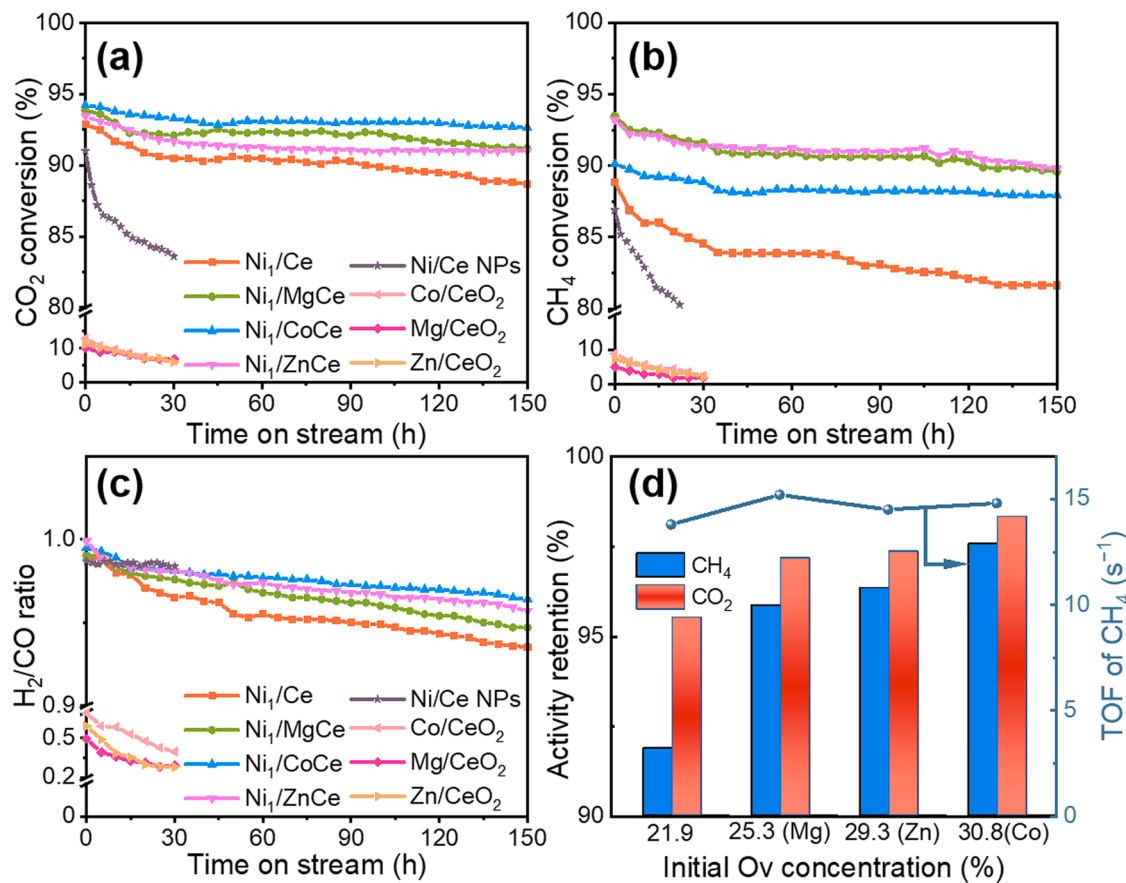


Fig. 5. Stability evaluation of catalysts for DRM reaction. (a) CO₂ conversion, (b) CH₄ conversion, and (c) H₂/CO ratio of the employed catalysts as a function of time on stream. (d) The activity retention after 150-h on stream and TOF of CH₄ with various O_v concentrations (O_v concentration was calculated from the *in-situ* XPS results). Reaction conditions: atmospheric pressure, T = 800 °C, CH₄/CO₂/Ar = 1/1/3, m_{cat.} = 0.1 g, GHSV = 30000 mL g⁻¹ h⁻¹, the activity retention was calculated by the ratio of initial conversion to final conversion.

catalysts in Fig. 6c. In addition, a few H₂O is originated from the reaction between CH₄ or H₂ and oxygen species. Here, the oxygen species consist of lattice oxygen (O_L) species and adsorbed oxygen (O_{ad}) species. Wherein, amount of O_L species over the Ni₁/MCe (M=Mg, Co, and Zn) catalysts are similar because the Ni₁/MCe catalysts have the similar Ni loadings, similar M loadings, similar SMSI, and similar CO-DRIFT spectra. Therefore, the catalyst with more O_{ad} species exhibited more H₂O evolution. It suggests the outstanding capacity of O_v on carbon removal along with CH₄ dissociation.

CO₂ activation is also a crucial step for carbon removal in the DRM process. In CO₂-TPSR experiments, CO₂ was activated and dissociated on O_v to produce O_{ad} species [50,51]. More O_v provided more adsorptive sites for CO₂ activation to produce more CO and O_{ad} species. The amount of CO₂ consumption and CO evolution of employed catalysts follow the same order as O_v concentration, indicating that the O_v are favorable for CO₂ activation (Fig. 7a-b). In addition, no CO₂ consumption signal was observed on the Ni/Ce NPs, suggesting the low O_v concentration on it. This also confirmed that the α' peak of the Ni/Ce NPs is not the reduction of O_{ad} species in the H₂-TPR results. After CO₂-TPSR, the H₂-TPR experiments were conducted to determine the amount of O_{ad} on O_v. It is obvious that catalysts with more O_v consumed more H₂. The amount of produced H₂O and H₂ consumption on samples follow the same order as O_v concentration, manifesting that O_v were filled with O_{ad} species derived from CO₂ activation. It demonstrates that O_v plays a key role in CO₂ activation.

3.4. Mechanism of carbon removal on O_v

The effect of O_v in DRM was investigated by the *in-situ* sequential pulse experiments. The catalysts were pre-reduced at 600 °C and injected with series of pulses of CH₄ and CO₂ at 800 °C to simulate the actual reaction condition. It is obvious that all the catalysts were suffered from carbon deposition during multiple CH₄ pulses and regenerated by sequential CO₂ pulses (Fig. 8a-d). During the first three pulses, the superior activity on Ni₁/MCe catalysts resulted in weaker CH₄ peaks and higher H₂ signals compared with Ni₁/Ce. Within the nine pulses of CH₄ stage, the amount of decomposed CH₄ is inhibited by the carbon deposition obviously. During the following three CO₂ pulses, catalysts with more O_v activated more CO₂ to form O_{ad} and then produce CO (Fig. 8c and d). The O_{ad} effectively removed deposited carbon and recovered the activity. Thus, in the last following CH₄ pulse, the catalysts with more O_v exhibited smaller CH₄ peaks, confirming the increase of O_v can improve the catalytic stability. It accords well with the stability evaluation results shown in Fig. 5.

Furthermore, each component in the effluent gas during the first nine pulses of CH₄ was quantified in Table S7-10. The coke deposition derived from the deep dissociation of CH₄ and resulted in deactivation (verified by the decline of H₂ formation amount). Active O_{ad} species on O_v sites reacted with the deposited carbon to produce CO and CO₂ so that the amount of O_{ad} consumption can be calculated by the produced CO and CO₂ (Eq. S7). The coke amount during each CH₄ pulses were calculated by the difference between CH₄ consumption and the CO evolution and CO₂ evolution (details are shown in Table S10 in the supporting information). The calculated total amount of O_{ad}

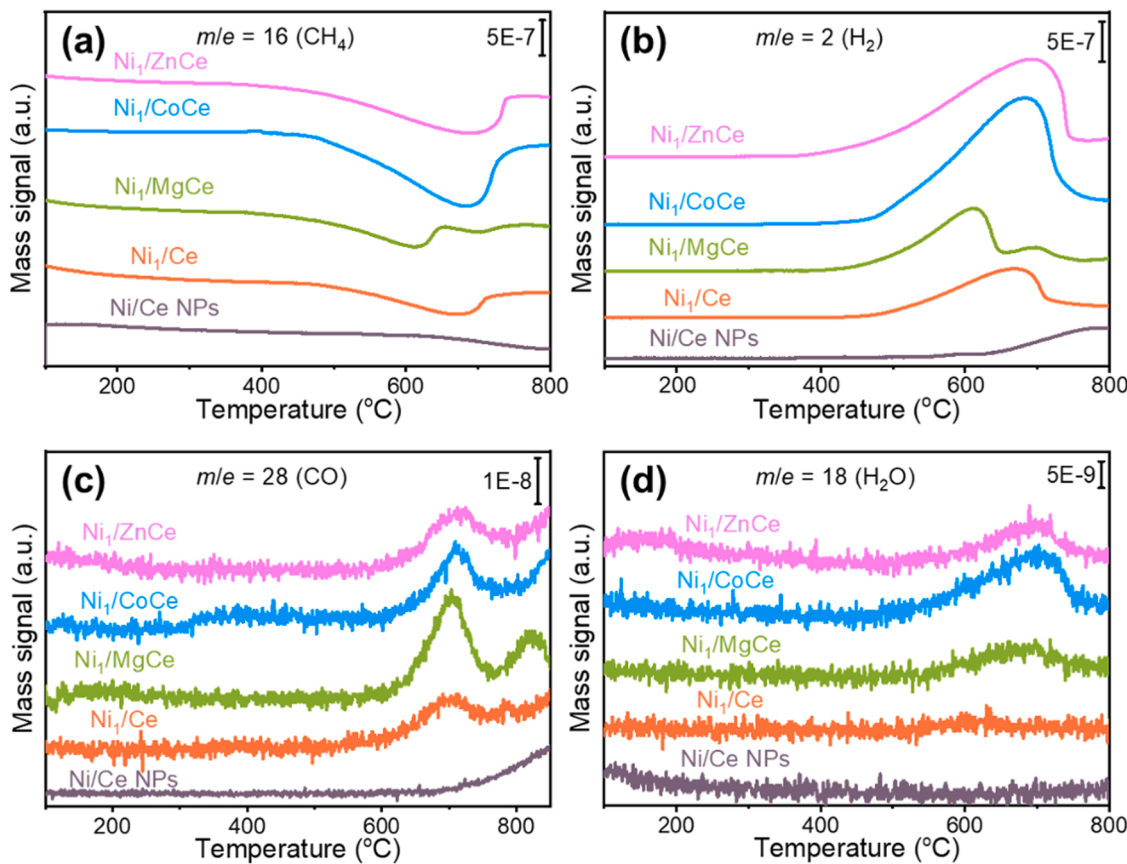


Fig. 6. (a) CH_4 , (b) H_2 , (c) CO and (d) H_2O signals of reduced catalysts during CH_4 -TPSR.

consumption (mmol) over catalysts followed the sequence: Ni_1/CoCe (0.1069) > Ni_1/ZnCe (0.1062) > Ni_1/MgCe (0.1051) > Ni_1/Ce (0.1023), which is consistent with the XPS and Raman results for the calculation for O_V . During the first three pulses, few cokes were accumulated due to the removal effect of abundant O_{ad} species on coke accumulation, which coincided with the high CH_4 consumption amount. The coke mainly accumulated at 3rd to 7th pulses (Fig. 8f), corresponding to the dramatical decline of O_{ad} species consumption amount at 3rd to 7th pulses (Fig. 8e). As for the 7th to 9th pulse, a few deposited carbon was accumulated because of the low activation of CH_4 .

Therefore, it demonstrates that atomically dispersed Ni atoms efficiently dissociate CH_4 and form undesirable carbon deposition. Meanwhile, O_V activates CO_2 to produce CO and O_{ad} species, which is in favor of carbon removal and activity retaining (Fig. 9a). This synergistic effect in the O_V -Ni SAC catalytic system maintained high activity in DRM reaction.

To further verify the mechanism of O_V formation and the carbon removal on O_V , the DFT calculations were carried out. The formation energy of O_V (E_V) and adsorption energy (E_{ads}) of CO_2 on CeO_2 with a second metal was investigated by DFT calculations. The E_V and E_{ads} was calculated by Eqs. (S8) and (S9) and shown in Fig. 9b. It is obvious that E_V of CeO_2 with a second metal follows the order: $\text{CoCe} < \text{ZnCe} < \text{MgCe} < \text{pure CeO}_2$, indicating that Co is the most favorable for the formation of O_V . In addition, the catalyst with more O_V exhibits lower E_{ads} in Fig. 9b, suggesting that O_V are the favorable active sites for CO_2 adsorption and activation.

According to TEM images of the spent catalysts, the CeO_2 nanorod were destroyed during DRM reaction. Obviously, Ni atoms were aggregated and carbon nanotubes were formed on the Ni/Ce NPs and Ni_1/Ce catalysts (Fig. 10a). In addition, the carbon nanotubes on Ni_1/Ce are obviously less than those on Ni/Ce NPs because it is hard to dissociated CH_4 deeply on Ni single atoms [8]. However, a few carbon

nanotubes were still formed on the Ni_1/Ce catalyst due to the aggregation of a few Ni atoms and resulted in catalyst deactivation (Fig. 10b). Besides, Ni 2p signals of the spent Ni_1/Ce catalyst are much higher than that of the fresh Ni_1/Ce catalysts (Fig. S6), confirming that Ni atoms were aggregated on the surface. On the contrary, no Ni NP was observed on the Ni_1/CoCe catalyst, indicating that isolated Ni atoms on the Ni_1/CoCe catalyst were stable during DRM reaction (Fig. 10c). Compared with the Ni_1/Ce catalyst, no carbon deposited on the Ni_1/CoCe catalyst, suggesting that the carbon deposition was inhibited along with the increase of O_V concentration. From the XRD spectra of the spent catalysts (Fig. 10e), no NiO signal was detected, suggesting the Ni single atoms were uneasy to be aggregated during the DRM reaction. Besides, the lattice parameters of the spent catalysts were calculated and shown in Fig. 10f. Compared with the fresh catalysts, the spent catalysts exhibited similar lattice parameters. Wherein, the Ni_1/CoCe catalyst showed the smallest lattice parameter and the largest peak shift. It demonstrated that the lattice contraction induced by the doping of Co is stable during the DRM reaction.

To investigate the graphite degree of deposited carbon, Raman spectra were conducted (Fig. 11a). It is reported that the value of I_G/I_D represents the graphite degree of carbon deposition and the graphite carbon is too inert to remove [52]. The calculated value of I_G/I_D shows a reverse sequence to O_V concentration, indicating more O_V led to the lower graphite degree. Especially, no obvious peaks are observed on the spent Ni_1/CoCe catalyst with the highest O_V concentration. Obvious mass losses on these catalysts in TG profiles can be attributed to the oxidation of carbon deposition (Fig. 11b). The mass loss amount on Ni_1/CoCe catalyst with the highest O_V concentration is negligible, indicating less carbon was accumulated on the catalysts with higher O_V concentration. To quantify the coke amount, O_2 -TPO experiments were also conducted (Fig. 11c and d). The higher formation temperature of CO and CO_2 evolution on the Ni_1/MgCe sample demonstrated that the

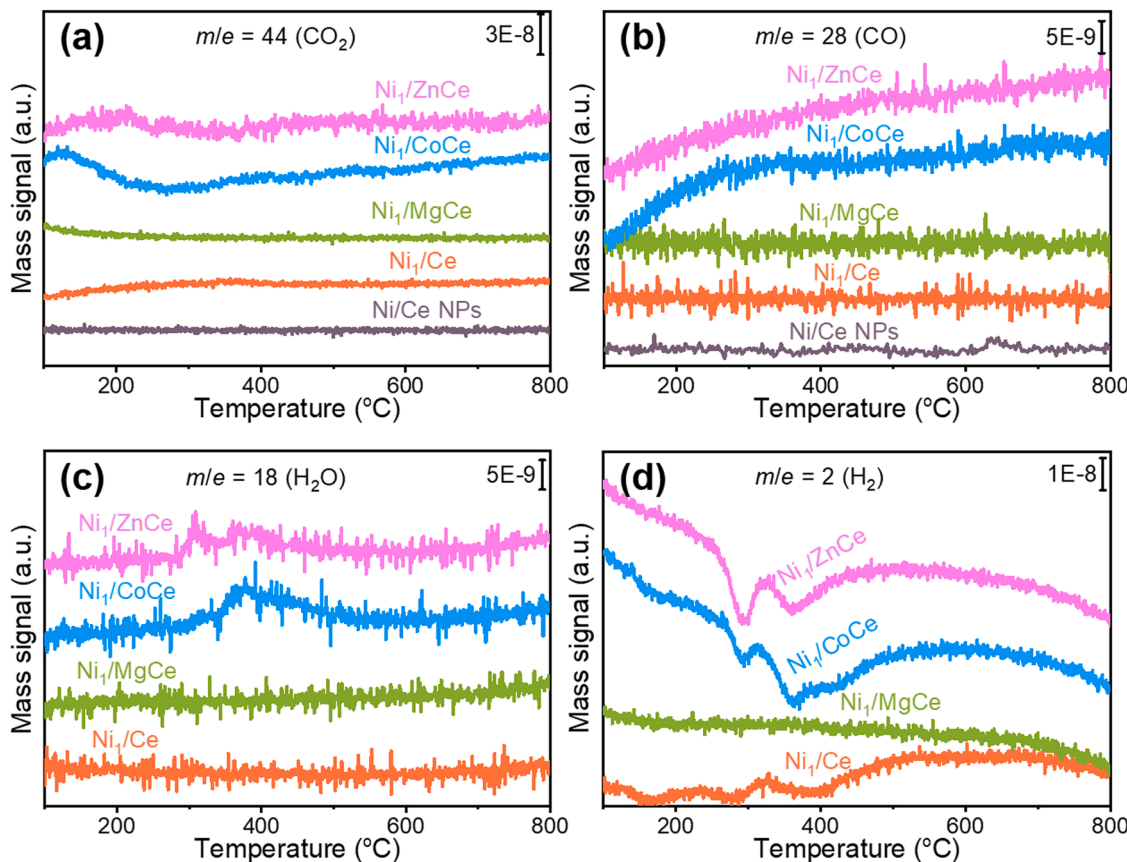


Fig. 7. (a) CO_2 and (b) CO signals of the reduced catalysts during CO_2 -TPSR. (c) H_2O and (d) H_2 signals during a H_2 -TPR experiments after CO_2 -TPSR.

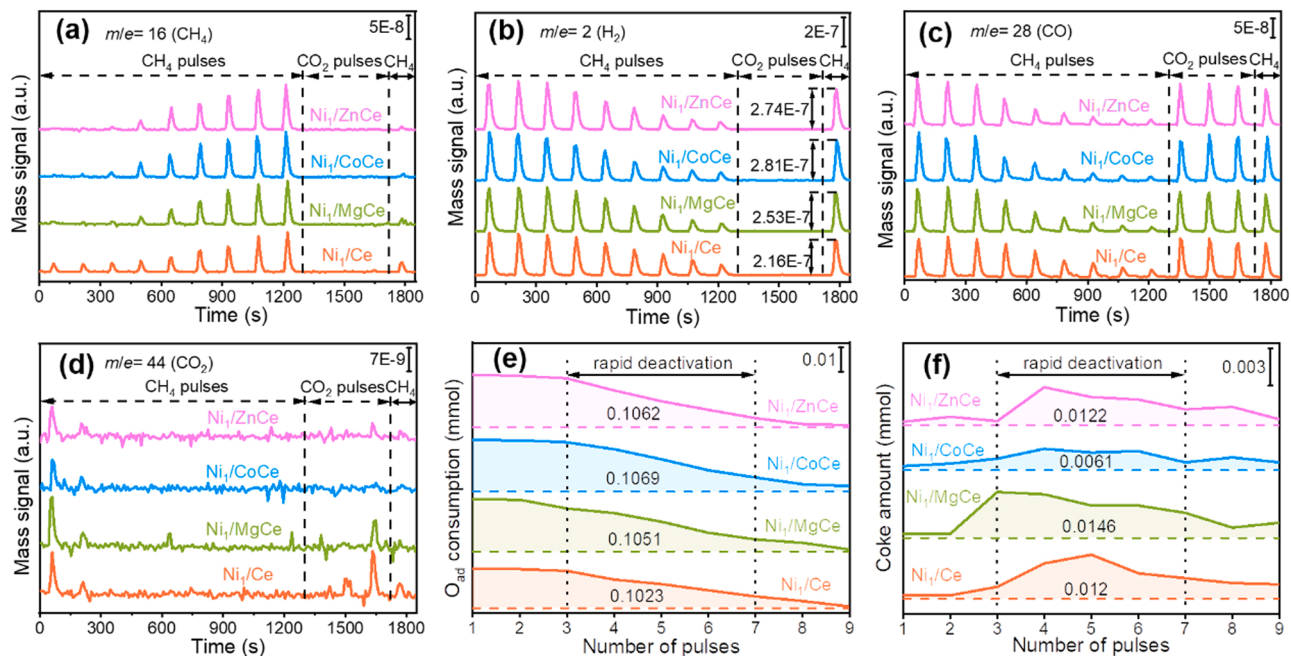


Fig. 8. (a) CH_4 , (b) H_2 , (c) CO and (d) CO_2 signals during pulse experiments. (e) Calculated O_{ad} consumption and (f) coke amount during each CH_4 pulses.

deposited carbon on Ni_1/MgCe is more inert than that on Ni_1/ZnCe and Ni_1/CoCe catalysts (verified by Raman and TG results). The carbon accumulation amount was measured in Table S12. Notably, catalysts with more O_V exhibited less carbon deposition. Wherein, no obvious coke signals were detected on Ni_1/CoCe with the most O_V , suggesting

the suppression effect of O_V on carbon deposition. It confirms that more O_V resulted in less carbon deposition.

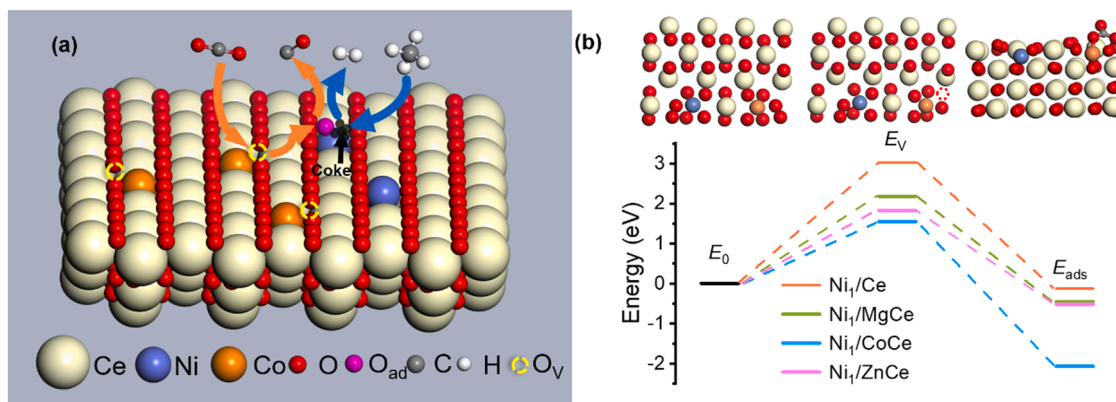


Fig. 9. (a) Schematic of the mechanism of carbon removal on O_v ; (b) The formation energy of O_v and adsorption energy of CO_2 on modified CeO₂(110), the E_0 represents the initial-state energy of CeO₂(110) modified by a second metal.

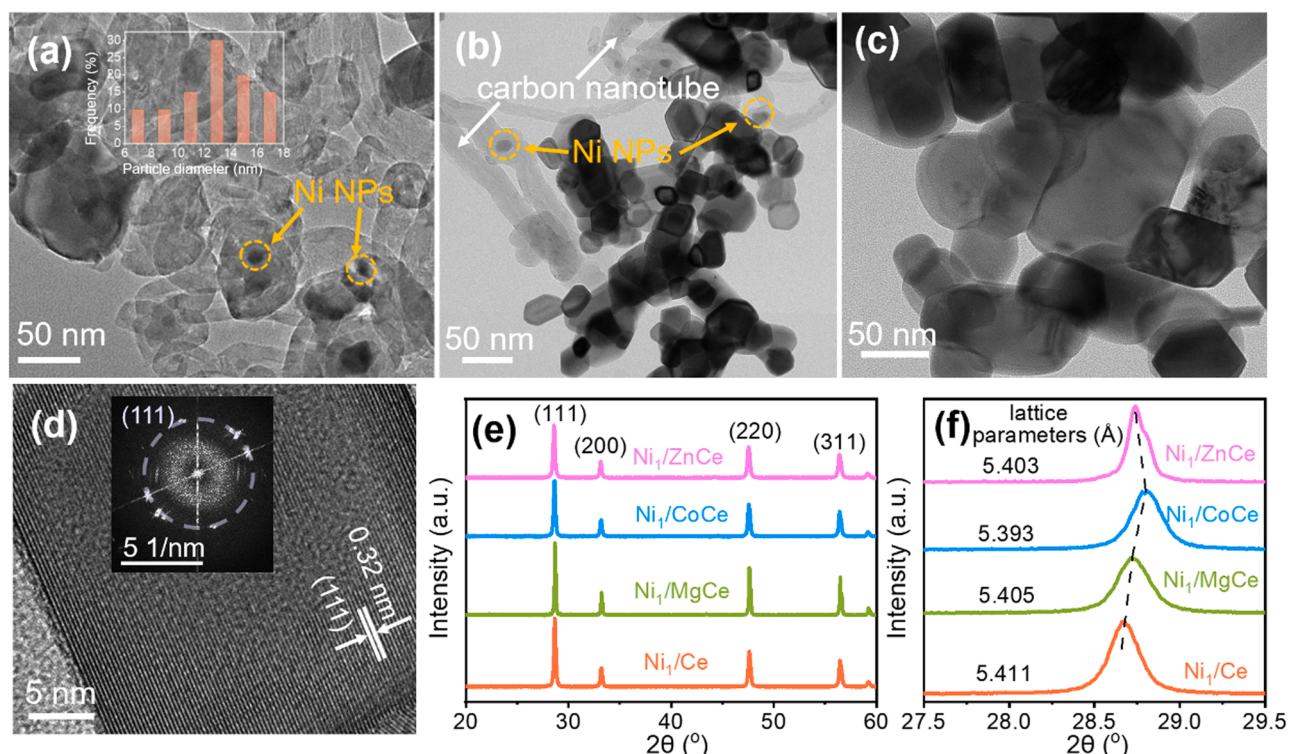


Fig. 10. TEM image of the spent (a) Ni/Ce NPs, (b) Ni₁/Ce, and (c and d) Ni₁/CoCe catalysts after 150 h DRM reaction. XRD patterns with (e) the region of 20 at 20–60° and (f) the region of 20 at 27.5–29.5° of the spent samples, the inset values are lattice parameters of CeO₂.

4. Conclusion

In summary, we synthesized O_v -rich Ni₁/M CeO₂ SACs with high activity and remarkable stability, and the O_v concentration was successfully regulated on CeO₂ by introducing a smaller-size metal cation. During the DRM process, isolated Ni atoms exhibit high CH₄ dissociation activity but suffered from rapid deactivation caused by the carbon deposition. O_v were confirmed as the active sites for CO₂ activation to produce O_{ad} , which simultaneously removed the carbon deposition and sustained the high activity. The catalyst with the highest O_v concentration (30.8%) performed the highest activity retention (96.5%) after 150 h DRM reaction and exhibited both extremely high stability and activity compared with other reported counterpart catalysts. By constructing this O_v -SAC model catalyst, the Ni single atoms maintain high activity for 150 h at 800 °C. This research demonstrates the effect of O_v on enhancing the stability of Ni SACs and provides a meaningful

reference to design catalysts with both high activity and stability for C-H activation.

CRediT authorship contribution statement

Jinwei Wu: Investigation, Validation, Formal analysis, Writing – original draft, DFT calculations, Writing – review & editing. **Jie Gao:** Conceptualization, Resources, Formal analysis, Writing – review & editing, Supervision. **Shuangshuang Lian:** Formal analysis. **Jianpeng Li:** Resources. **Kaihang Sun:** Writing – review & editing. **Shufang Zhao:** Formal analysis. **Young Dok Kim:** Formal analysis. **Yujing Ren:** Formal analysis. **Meng Zhang:** Formal analysis. **Qiaoyun Liu:** Formal analysis. **Zhongyi Liu:** Resources, Project administration. **Zhikun Peng:** Conceptualization, Formal analysis, Resources, Writing – review & editing, Funding acquisition, Supervision.

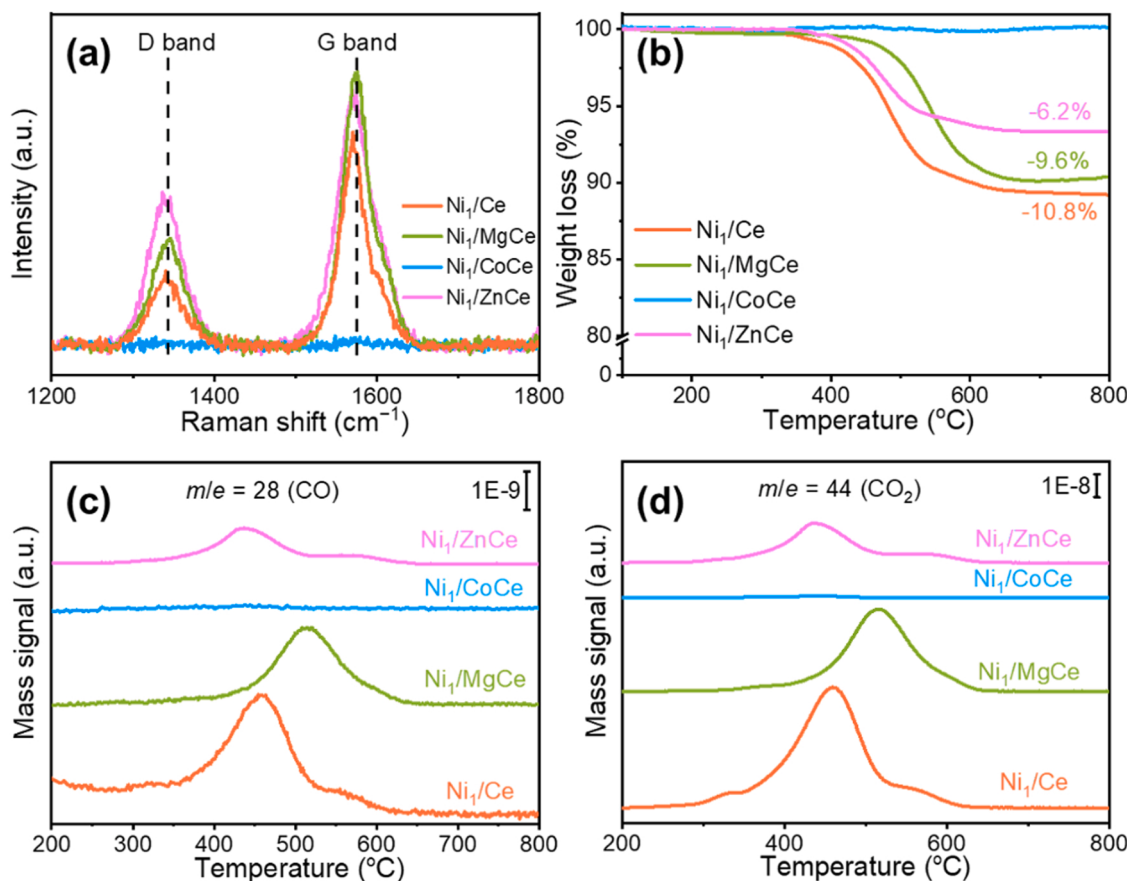


Fig. 11. (a, b) Raman spectra, TGA profiles and (c, d) O₂-TPO results of spent catalysts after 150 h DRM reaction.

Declaration of Competing Interest

The authors declare that they have no known competing financial interests or personal relationships that could have appeared to influence the work reported in this paper.

Acknowledgment

This work was supported by National Natural Science Foundation of China (No. 22172119, 21908203), the Natural Science Basic Research Plan in Shaanxi Province of China (2021JM-047), China Postdoctoral Science Foundation (2021M692911), Science and Technology Project of Henan Province 212102210192, and Central Plains Science and Technology Innovation Leader Project (No. 241200510006). We thank Dr. Dan Feng (Analytical & Testing Center, Northwestern Polytechnical University, Xi'an) for her help on the AC-HAADF-STEM testing. We also acknowledge Professor Wei Liu (Dalian National Laboratory for Clean Energy, DICP, Dalian) for fruitful discussion on the AC-HAADF-STEM results.

Appendix A. Supporting information

Supplementary data associated with this article can be found in the online version at [doi:10.1016/j.apcatb.2022.121516](https://doi.org/10.1016/j.apcatb.2022.121516).

References

- [1] J. Wencel-Delord, F. Glorius, C-H bond activation enables the rapid construction and late-stage diversification of functional molecules, *Nat. Chem.* 5 (2013) 369–375.
- [2] J.A. Labinger, J.E. Bercaw, Understanding and exploiting C-H bond activation, *Nature* 417 (2002) 507–514.
- [3] P.G. Lustemberg, R.M. Palomino, R.A. Gutierrez, D.C. Griner, M. Vorokhta, Z. Liu, P.J. Ramirez, V. Matolin, M. Veronica Ganduglia-Pirovano, S.D. Senanayake, J. A. Rodriguez, Direct conversion of methane to methanol on Ni-ceria surfaces: metal-support interactions and water-enabled catalytic conversion by site blocking, *J. Am. Chem. Soc.* 140 (2018) 7681–7687.
- [4] D.C. Upman, V. Agarwal, A. Khechfe, Z.R. Snodgrass, M.J. Gordon, H. Metiu, E. W. McFarland, Catalytic molten metals for the direct conversion of methane to hydrogen and separable carbon, *Science* 358 (2017) 917–920.
- [5] J.J. Shan, J.L. Liu, M.W. Li, S. Lustig, S. Lee, M. Flytzani-Stephanopoulos, NiCu single atom alloys catalyze the C-H bond activation in the selective non-oxidative ethanol dehydrogenation reaction, *Appl. Catal. B Environ.* 226 (2018) 534–543.
- [6] F.G. Wang, B.L. Han, L.J. Zhang, L.L. Xu, H. Yu, W.D. Shi, CO₂ reforming with methane over small-sized Ni/SiO₂ catalysts with unique features of sintering-free and low carbon, *Appl. Catal. B Environ.* 235 (2018) 26–35.
- [7] K.H. Han, Y. Wang, S. Wang, Q.Y. Liu, Z.Y. Deng, F.G. Wang, Narrowing band gap energy of CeO₂ in (Ni/CeO₂)@SiO₂ catalyst for photothermal methane dry reforming, *Chem. Eng. J.* 421 (2021), 129989.
- [8] M. Akri, S. Zhao, X.Y. Li, K.T. Zang, A.F. Lee, M.A. Isaacs, W. Xi, Y. Gangarajula, J. Luo, Y.J. Ren, Y.T. Cui, L. Li, Y. Su, X.L. Pan, W. Wen, Y. Pan, K. Wilson, L. Li, B. T. Qiao, H. Ishii, Y.F. Liao, A.Q. Wang, X.D. Wang, T. Zhang, Atomically dispersed nickel as coke-resistant active sites for methane dry reforming, *Nat. Commun.* 10 (2019) 10.
- [9] B.T. Qiao, A.Q. Wang, X.F. Yang, L.F. Allard, Z. Jiang, Y.T. Cui, J.Y. Liu, J. Li, T. Zhang, Single-atom catalysis of CO oxidation using Pt₁/FeO_x, *Nature Chem.* 3 (2011) 634–641.
- [10] Y. Song, E. Ozdemir, S. Ramesh, A. Adishev, S. Subramanian, A. Harale, M. Albuali, B.A. Fadhel, A. Jamal, D. Moon, S.H. Choi, C.T. Yavuz, Dry reforming of methane by stable Ni-Mo nanocatalysts on single-crystalline MgO, *Science* 367 (2020) 777–781.
- [11] M.S. Li, A.C. van Veen, Tuning the catalytic performance of Ni-catalysed dry reforming of methane and carbon deposition via Ni-CeO_{2-x} interaction, *Appl. Catal. B Environ.* 237 (2018) 641–648.
- [12] D. Baudouin, U. Rodemerck, F. Krumeich, A. de Mallmann, K.C. Szeto, H. Menard, L. Veyre, J.-P. Candy, P.B. Webb, C. Thieuleux, C. Copret, Particle size effect in the low temperature reforming of methane by carbon dioxide on silica-supported Ni nanoparticles, *J. Catal.* 297 (2013) 27–34.
- [13] Z.J. Zuo, S.Z. Liu, Z.C. Wang, C. Liu, W. Huang, J. Huang, P. Liu, Dry reforming of methane on single-site Ni/MgO catalysts: importance of site confinement, *ACS Catal.* 8 (2018) 9821–9835.
- [14] M.D. Marcinkowski, M.T. Darby, J.L. Liu, J.M. Wimble, F.R. Lucci, S. Lee, A. Michaelides, M. Flytzani-Stephanopoulos, M. Stamatakis, E.C.H. Sykes, Pt/Cu

- single-atom alloys as coke-resistant catalysts for efficient C-H activation, *Nat. Chem.* 10 (2018) 325–332.
- [15] K.H. Han, S.Y. Xu, Y. Wang, S. Wang, L. Zhao, J. Kamponde, H. Yu, W.D. Shi, F. G. Wang, Confining Ni and ceria in silica shell as synergistic multifunctional catalyst for methane dry reforming reaction, *J. Power Sources* 506 (2021), 230232.
- [16] X.W. Liu, K.B. Zhou, L. Wang, B.Y. Wang, Y.D. Li, Oxygen vacancy clusters promoting reducibility and activity of ceria nanorods, *J. Am. Chem. Soc.* 131 (2009) 3140–3141.
- [17] F.G. Wang, Y. Wang, L.J. Zhang, J.Y. Zhu, B.L. Han, W.Q. Fan, L.L. Xu, H. Yu, W. J. Cai, Z.C. Li, Z.Y. Deng, W.D. Shi, Performance enhancement of methane dry reforming reaction for syngas production over Ir/Ce_{0.9}La_{0.1}O₂-nanorods catalysts, *Catal. Today* 355 (2020) 502–511.
- [18] F. Carraro, A. Papohunda, M.C. Paganini, S. Agnoli, Morphology and size effect of ceria nanostructures on the catalytic performances of Pd/CeO₂ catalysts for methanol decomposition to syngas, *ACS Appl. Nano Mater.* 1 (2018) 1492–1501.
- [19] Y.-Q. Su, I.A.W. Filot, J.-X. Liu, E.J.M. Hensgen, Stable Pd-doped ceria structures for CH₄ activation and CO oxidation, *ACS Catal.* 8 (2018) 75–80.
- [20] Y.F. Wang, Z. Chen, P. Han, Y.H. Du, Z.X. Gu, X. Xu, G.F. Zheng, Single-atomic Cu with multiple oxygen vacancies on ceria for electrocatalytic CO₂ reduction to CH₄, *ACS Catal.* 8 (2018) 7113–7119.
- [21] F. Esch, S. Fabris, L. Zhou, T. Montini, C. Africh, P. Fornasiero, G. Comelli, R. Rosei, Electron localization determines defect formation on ceria substrates, *Science* 309 (2005) 752–755.
- [22] Y. Tang, Y. Wei, Z. Wang, S. Zhang, Y. Li, L. Nguyen, Y. Li, Y. Zhou, W. Shen, F. Tao, P. Hu, Synergy of single-atom Ni₁ and Ru₁ sites on CeO₂ for dry reforming of CH₄, *J. Am. Chem. Soc.* 141 (2019) 7283–7293.
- [23] C.M. Yang, Y.X. Lu, L. Zhang, Z.J. Kong, T.Y. Yang, L. Tao, Y.Q. Zou, S.Y. Wang, Defect Engineering on CeO₂-Based Catalysts for Heterogeneous Catalytic Applications, *Small Struct.* 2 (2021) 2100058.
- [24] X.Q. Wang, J.C. Hanson, J.A. Rodriguez, C. Belver, M. Fernandez-Garcia, The structural and electronic properties of nanostructured Ce_{1-x}Zr_xTb_yO₂ ternary oxides. Unusual concentration of Tb³⁺ and metal <-> oxygen <-> metal interactions, *J. Chem. Phys.* 122 (2005), 154711.
- [25] S. Das, A. Jangam, S. Jayaprakash, S.B. Xi, K. Hidajat, K. Tomishige, S. Kawi, Role of lattice oxygen in methane activation on Ni-phyllosilicate@Ce_{1-x}Zr_xO₂ core-shell catalyst for methane dry reforming: Zr doping effect, mechanism, and kinetic study, *Appl. Catal. B Environ.* 290 (2021), 119998.
- [26] Z. Zhang, J. Li, W. Gao, Y. Ma, Y. Qu, Pt/porous nanorods of ceria as efficient high temperature catalysts with remarkable catalytic stability for carbon dioxide reforming of methane, *J. Mater. Chem. A* 3 (2015) 18074–18082.
- [27] G.I. Siakvelas, N.D. Charisiou, S. Alkhoori, A.A. Alkhoori, V. Sebastian, S. J. Hinder, M.A. Baker, I.V. Yentekakis, K. Polychronopoulou, M.A. Goula, Highly selective and stable nickel catalysts supported on ceria promoted with Sm₂O₃, Pr₂O₃ and MgO for the CO₂ methanation reaction, *Appl. Catal. B Environ.* 282 (2021), 119562.
- [28] J. Lin, C. Ma, Q. Wang, Y. Xu, G. Ma, J. Wang, H. Wang, C. Dong, C. Zhang, M. Ding, Enhanced low-temperature performance of CO₂ methanation over mesoporous Ni/Al₂O₃-ZrO₂ catalysts, *Appl. Catal. B Environ.* 243 (2019) 262–272.
- [29] B. Liu, C.M. Li, G.Q. Zhang, X.S. Yao, S.S.C. Chuang, Z. Li, Oxygen vacancy promoting dimethyl carbonate synthesis from CO₂ and methanol over Zr-doped CeO₂ nanorods, *ACS Catal.* 8 (2018) 10446–10456.
- [30] N. Wang, K. Shen, L. Huang, X. Yu, W. Qian, W. Chu, Facile route for synthesizing ordered mesoporous Ni-Ce-Al oxide materials and their catalytic performance for methane dry reforming to hydrogen and syngas, *ACS Catal.* 3 (2013) 1638–1651.
- [31] H. Liu, Z.X. Fan, C.Z. Sun, S.H. Yu, S. Feng, W. Chen, D.Z. Chen, C.J. Tang, F. Gao, L. Dong, Improved activity and significant SO₂ tolerance of samarium modified CeO₂-TiO₂ catalyst for NO selective catalytic reduction with NH₃, *Appl. Catal. B Environ.* 244 (2019) 671–683.
- [32] R.P. Ye, Q.H. Li, W.B. Gong, T.T. Wang, J.J. Razink, L. Lin, Y.Y. Qin, Z.F. Zhou, H. Adidharma, J.K. Tang, A.G. Russell, M.H. Fan, Y.G. Yao, High-performance of nanostructured Ni/CeO₂ catalyst on CO₂ methanation, *Appl. Catal. B Environ.* 268 (2020), 118474.
- [33] D. Guo, Y. Lu, Y.Z. Ruan, Y.F. Zhao, Y.J. Zhao, S.P. Wang, X.B. Ma, Effects of extrinsic defects originating from the interfacial reaction of CeO_{2-x}-nickel silicate on catalytic performance in methane dry reforming, *Appl. Catal. B Environ.* 277 (2020), 119278.
- [34] X.H. Zheng, Y.L. Li, L.Y. Zhang, L.J. Shen, Y.H. Xiao, Y.F. Zhang, C.T. Au, L. L. Jiang, Insight into the effect of morphology on catalytic performance of porous CeO₂ nanocrystals for H₂S selective oxidation, *Appl. Catal. B Environ.* 252 (2019) 98–110.
- [35] P. Zhao, F. Qin, Z. Huang, C. Sun, W. Shen, H.L. Xu, Morphology-dependent oxygen vacancies and synergistic effects of Ni/CeO₂ catalysts for N₂O decomposition, *Catal. Sci. Technol.* 8 (2018) 276–288.
- [36] J.J. Kong, Z.W. Xiang, G.Y. Li, T.C. An, Introduce oxygen vacancies into CeO₂ catalyst for enhanced coke resistance during photothermocatalytic oxidation of typical VOCs, *Appl. Catal. B Environ.* 269 (2020), 118755.
- [37] Y.C. Zhang, Z. Li, L. Zhang, L. Pan, X.W. Zhang, L. Wang, A. Fazale, J.J. Zou, Role of oxygen vacancies in photocatalytic water oxidation on ceria oxide: Experiment and DFT studies, *Appl. Catal. B Environ.* 224 (2018) 101–108.
- [38] J.W. Han, J.S. Park, M.S. Choi, H. Lee, Uncoupling the size and support effects of Ni catalysts for dry reforming of methane, *Appl. Catal. B* 203 (2017) 625–632.
- [39] G. Zhou, H. Liu, K. Cui, A. Jia, G. Hu, Z. Jiao, Y. Liu, X. Zhang, Role of surface Ni and Ce species of Ni/CeO₂ catalyst in CO₂ methanation, *Appl. Surf. Sci.* 383 (2016) 248–252.
- [40] M. Zhang, J. Zhang, Z. Zhou, S. Chen, T. Zhang, F. Song, Q. Zhang, N. Tsubaki, Y. Tan, Y. Han, Effects of the surface adsorbed oxygen species tuned by rare-earth metal doping on dry reforming of methane over Ni/ZrO₂ catalyst, *Appl. Catal. B Environ.* 264 (2020).
- [41] S. Das, S. Bhattar, L.N. Liu, Z.G. Wang, S.B. Xi, J.J. Spivey, S. Kawi, Effect of partial Fe substitution in La_{0.9}Sr_{0.1}NiO₃ perovskite-derived catalysts on the reaction mechanism of methane dry reforming, *ACS Catal.* 10 (2020) 12466–12486.
- [42] S. Dama, S.R. Ghodke, R. Bobade, H.R. Gurav, S. Chilukuri, Active and durable alkaline earth metal substituted perovskite catalysts for dry reforming of methane, *Appl. Catal. B Environ.* 224 (2018) 146–158.
- [43] J.L. Rogers, M.C. Mangarella, A.D. D'Amico, J.R. Gallagher, M.R. Dutzer, E. Stavitski, J.T. Miller, C. Sievers, Differences in the nature of active sites for methane dry reforming and methane steam reforming over nickel aluminate catalysts, *ACS Catal.* 6 (2016) 5873–5886.
- [44] K. Song, M.M. Lu, S.P. Xu, C.Q. Chen, Y.Y. Zhan, D.L. Li, C. Au, L.L. Jiang, K. Tomishige, Effect of alloy composition on catalytic performance and coke-resistance property of Ni-Cu/Mg(Al)O catalysts for dry reforming of methane, *Appl. Catal. B Environ.* 239 (2018) 324–333.
- [45] F.G. Wang, L.L. Xu, W.D. Shi, J. Zhang, K. Wu, Y. Zhao, H. Li, H.X. Li, G.Q. Xu, W. Chen, Thermally stable Ir/Ce_{0.9}La_{0.1}O₂ catalyst for high temperature methane dry reforming reaction, *Nano Res.* 10 (2017) 364–380.
- [46] J. Dou, R. Zhang, X. Hao, Z. Bao, T. Wu, B. Wang, F. Yu, Sandwiched SiO₂@Ni@ZrO₂ as a coke resistant nanocatalyst for dry reforming of methane, *Appl. Catal. B Environ.* 254 (2019) 612–623.
- [47] S. Das, J. Ashok, Z. Bian, N. Dewangan, M.H. Wai, Y. Du, A. Borgna, K. Hidajat, S. Kawi, Silica-ceria sandwiched Ni core-shell catalyst for low temperature dry reforming of biogas: coke resistance and mechanistic insights, *Appl. Catal. B Environ.* 230 (2018) 220–236.
- [48] J. Wei, E. Iglesia, Isotopic and kinetic assessment of the mechanism of reactions of CH₄ with CO₂ or H₂O to form synthesis gas and carbon on nickel catalysts, *J. Catal.* 224 (2004) 370–383.
- [49] P.G. Lustemberg, P.J. Ramirez, Z. Liu, R.A. Gutierrez, D.G. Grinter, J. Carrasco, S. D. Senanayake, J.A. Rodriguez, M. Veronica Ganduglia-Pirovano, Room-temperature activation of methane and dry re-forming with CO₂ on Ni-CeO₂(111) surfaces: effect of Ce³⁺ sites and metal-support interactions on C-H bond cleavage, *ACS Catal.* 6 (2016) 8184–8191.
- [50] D.K. Kim, K. Stoeve, F. Mueller, W.F. Maier, Mechanistic study of the unusual catalytic properties of a new Ni-Ce mixed oxide for the CO₂ reforming of methane, *J. Catal.* 247 (2007) 101–111.
- [51] I.V. Yentekakis, G. Goula, M. Hatzisymeon, I. Betsi-Arygropoulou, G. Botzolaki, K. Kousi, D.I. Kondarides, M.J. Taylor, C.M.A. Parlett, A. Osatishtiani, G. Kyriakou, J.P. Holgado, R.M. Lambert, Effect of support oxygen storage capacity on the catalytic performance of Rh nanoparticles for CO₂ reforming of methane, *Appl. Catal. B Environ.* 243 (2019) 490–501.
- [52] K.H. Han, W.S. Yu, L.L. Xu, Z.Y. Deng, H. Yu, F.G. Wang, Reducing carbon deposition and enhancing reaction stability by ceria for methane dry reforming over Ni@SiO₂@CeO₂ catalyst, *Fuel* 291 (2021), 120182.